

Regularization by Denoising: Clarifications and New Interpretations

Edward T. Reehorst and Philip Schniter, *Fellow, IEEE*

Abstract—Regularization by Denoising (RED), as recently proposed by Romano, Elad, and Milanfar, is powerful new image-recovery framework that aims to construct an explicit regularization objective from a plug-in image-denoising function. Evidence suggests that the RED algorithms are, indeed, state-of-the-art. However, a closer inspection suggests that explicit regularization may not explain the workings of these algorithms. In this paper, we clarify that the expressions in Romano et al. hold only when the denoiser has a symmetric Jacobian, and we demonstrate that such symmetry does not occur with practical denoisers such as non-local means, BM3D, TNRD, and DnCNN. Going further, we prove that non-symmetric denoising functions cannot be modeled by any explicit regularizer. In light of these results, there remains the question of how to justify the good-performing RED algorithms for practical denoisers. In response, we propose a new framework called “score-matching by denoising” (SMD), which aims to match the score (i.e., the gradient of the log-prior) instead of designing the regularizer itself. We also show tight connections between SMD, kernel density estimation, and constrained minimum mean-squared error denoising. Finally, we provide new interpretations of the RED algorithms proposed by Romano et al., and we propose novel RED algorithms with faster convergence.

I. INTRODUCTION

Consider the problem of recovering a (vectorized) image $\mathbf{x}^0 \in \mathbb{R}^N$ from noisy linear measurements $\mathbf{y} \in \mathbb{R}^M$ of the form

$$\mathbf{y} = \mathbf{A}\mathbf{x}^0 + \mathbf{e}, \quad (1)$$

where $\mathbf{A} \in \mathbb{R}^{M \times N}$ is a known linear transformation. This problem is of great importance in many applications and has been intensely studied for several decades. (See, e.g., the discussion in [1].)

One of the most popular approaches to image recovery is the “variational” approach, where one poses and solves an optimization problem of the form

$$\hat{\mathbf{x}} = \arg \min_{\mathbf{x}} \{ \ell(\mathbf{x}; \mathbf{y}) + \lambda \rho(\mathbf{x}) \}. \quad (2)$$

In (2), $\ell(\mathbf{x}; \mathbf{y})$ is a loss function that penalizes mismatch to the measurements, $\rho(\mathbf{x})$ is a regularization term that penalizes mismatch to the image class of interest, and $\lambda > 0$ is a design parameter that trades between loss and regularization. A prime advantage of the variational approach is that efficient, off-the-shelf optimization methods can be readily applied to (2).

E. T. Reehorst (email: reehorst.3@osu.edu) and P. Schniter (email: schniter.1@osu.edu) are with the Department of Electrical and Computer Engineering, The Ohio State University, Columbus, OH, 43210. Their work is supported in part by the National Science Foundation through grants CCF-1527162 and CCF-1716388.

A key question is: how should one choose the loss $\ell(\cdot; \mathbf{y})$ and regularization $\rho(\cdot)$ in (2)? As discussed in the sequel, the MAP-Bayesian interpretation suggests that they should be chosen in proportion to the negative log-likelihood and negative log-prior, respectively. The trouble is that efficient and accurate prior models of images are lacking.

Recently, a breakthrough was made by Romano, Elad, and Milanfar in [1]. Leveraging the relative maturity of image denoising algorithms (see, e.g., [2], [3]), they proposed the *regularization by denoising* (RED) framework, where an explicit regularizer $\rho(\mathbf{x})$ is constructed from an image denoiser $\mathbf{f} : \mathbb{R}^N \rightarrow \mathbb{R}^N$ using the simple and elegant rule

$$\rho_{\text{red}}(\mathbf{x}) = \frac{1}{2} \mathbf{x}^\top (\mathbf{x} - \mathbf{f}(\mathbf{x})). \quad (3)$$

Based on this framework, Romano et al. proposed several recovery algorithms (based on steepest descent, ADMM, and fixed-point methods, respectively) that yield state-of-the-art performance in deblurring and super-resolution tasks.

In this paper, we provide some clarifications and new interpretations of the excellent RED algorithms from [1]. Our work was motivated by an interesting empirical observation: with practical denoisers $\mathbf{f}(\cdot)$, the RED algorithms do not minimize the RED variational objective “ $\ell(\mathbf{x}; \mathbf{y}) + \lambda \rho_{\text{red}}(\mathbf{x})$.” As we establish in the sequel, the RED regularization (3) is justified only for denoisers with symmetric Jacobians, which unfortunately does not cover many state-of-the-art methods such as non-local means (NLM) [4], BM3D [5], TNRD [6], and DnCNN [7]. In fact, we are able to establish a stronger result: For non-symmetric denoisers, there exists no regularization $\rho(\cdot)$ that explains the RED algorithms from [1].

In light of these (negative) results, there remains the question of how to explain/understand the RED algorithms from [1] when used with non-symmetric denoisers. In response, we propose a framework called “score-matching by denoising” (SMD), which aims to match the *score* (i.e., the gradient of the log-prior) rather than to design any explicit regularizer. We then show tight connections between SMD, kernel density estimation [8], and constrained minimum mean-squared error (MMSE) denoising. Finally, we provide new interpretations of the RED-ADMM and RED-FP algorithms proposed in [1], and we propose novel RED algorithms with faster convergence.

The remainder of the paper is organized as follows. In Section II we provide more background on RED and related algorithms such as plug-and-play ADMM [9]. In Section III, we discuss the impact of Jacobian symmetry on RED and whether this property holds in practice. In Section IV, we propose the framework of “score-matching by denoising.” In Section V, we

present new interpretations of the RED-ADMM and RED-FP algorithms from [1], and we propose new algorithms based on Peaceman-Rachford splitting, expectation-consistent approximation, and majorization minimization. Finally, in Section VI, we conclude.

II. BACKGROUND

A. The MAP-Bayesian Interpretation

Because it will be useful in the sequel, we now provide a short discussion of Bayesian maximum a posteriori (MAP) estimation [10]. The MAP estimate of \mathbf{x} from \mathbf{y} is defined as

$$\hat{\mathbf{x}}_{\text{map}} = \arg \max_{\mathbf{x}} p(\mathbf{x}|\mathbf{y}), \quad (4)$$

where $p(\mathbf{x}|\mathbf{y})$ denotes the probability density of \mathbf{x} given \mathbf{y} . Notice that, from Bayes rule $p(\mathbf{x}|\mathbf{y}) = p(\mathbf{y}|\mathbf{x})p(\mathbf{x})/p(\mathbf{y})$ and the monotonically increasing nature of $\ln(\cdot)$, we can write

$$\hat{\mathbf{x}}_{\text{map}} = \arg \min_{\mathbf{x}} \{ -\ln p(\mathbf{y}|\mathbf{x}) - \ln p(\mathbf{x}) \}. \quad (5)$$

MAP estimation (5) has a direct connection to variation optimization (2): the log-likelihood term $-\ln p(\mathbf{y}|\mathbf{x})$ corresponds to the loss $\ell(\mathbf{x}; \mathbf{y})$ and the log-prior term $-\ln p(\mathbf{x})$ corresponds to the regularization $\lambda\rho(\mathbf{x})$. For example, with additive white Gaussian noise (AWGN) $\mathbf{e} \sim \mathcal{N}(0, \sigma_e^2 \mathbf{I})$, the log-likelihood implies a quadratic loss:

$$\ell(\mathbf{x}; \mathbf{y}) = \frac{1}{2\sigma_e^2} \|\mathbf{Ax} - \mathbf{y}\|^2. \quad (6)$$

Equivalently, the normalized loss $\ell(\mathbf{x}; \mathbf{y}) = \frac{1}{2} \|\mathbf{Ax} - \mathbf{y}\|^2$ could be used if σ_e^2 was absorbed into λ .

B. ADMM

A popular approach to solving (2) is through ADMM [11], which we now review. Using variable splitting, (2) becomes

$$\hat{\mathbf{x}} = \arg \min_{\mathbf{x}} \ell(\mathbf{x}; \mathbf{y}) + \lambda\rho(\mathbf{v}) \quad \text{s.t. } \mathbf{x} = \mathbf{v}, \quad (7)$$

which can be converted to the unconstrained problem

$$\arg \min_{\mathbf{x}, \mathbf{v}} \max_{\mathbf{p}} \ell(\mathbf{x}; \mathbf{y}) + \lambda\rho(\mathbf{v}) + \mathbf{p}^\top (\mathbf{x} - \mathbf{v}) + \frac{\beta}{2} \|\mathbf{x} - \mathbf{v}\|^2 \quad (8)$$

using Lagrange multipliers (or “dual” variables) \mathbf{p} and a design parameter $\beta > 0$. Using $\mathbf{u} \triangleq \mathbf{p}/\beta$, (8) can be simplified to

$$\arg \min_{\mathbf{x}, \mathbf{v}} \max_{\mathbf{u}} \ell(\mathbf{x}; \mathbf{y}) + \lambda\rho(\mathbf{v}) + \frac{\beta}{2} \|\mathbf{x} - \mathbf{v} + \mathbf{u}\|^2. \quad (9)$$

The ADMM algorithm solves (9) by alternating the optimization of \mathbf{x} , \mathbf{v} , and \mathbf{u} , as specified in Algorithm 1. ADMM is known to converge under convex $\ell(\cdot; \mathbf{y})$ and $\rho(\cdot)$ as well as other mild conditions (see [11]).

Algorithm 1 ADMM [11]

Require: $\ell(\cdot; \mathbf{y})$, $\rho(\cdot)$, β , λ , \mathbf{v}_0 , \mathbf{u}_0 , and K

- 1: **for** $k = 1, 2, \dots, K$ **do**
- 2: $\mathbf{x}_k = \arg \min_{\mathbf{x}} \{ \ell(\mathbf{x}; \mathbf{y}) + \frac{\beta}{2} \|\mathbf{x} - \mathbf{v}_{k-1} + \mathbf{u}_{k-1}\|^2 \}$
- 3: $\mathbf{v}_k = \arg \min_{\mathbf{v}} \{ \lambda\rho(\mathbf{v}) + \frac{\beta}{2} \|\mathbf{v} - \mathbf{x}_k - \mathbf{u}_{k-1}\|^2 \}$
- 4: $\mathbf{u}_k = \mathbf{u}_{k-1} + \mathbf{x}_k - \mathbf{v}_k$
- 5: **end for**
- 6: Return \mathbf{x}_K

C. Plug-and-Play ADMM

Importantly, line 3 of Algorithm 1 can be recognized as variational *denoising* of \mathbf{x} using regularization $\lambda\rho(\mathbf{x})$ and quadratic loss $\ell(\mathbf{x}; \mathbf{r}) = \frac{1}{2\nu} \|\mathbf{x} - \mathbf{r}\|^2$, where $\mathbf{r} = \mathbf{x}_k + \mathbf{u}_{k-1}$ at iteration k . Here “denoising” means recovering \mathbf{x}^0 from noisy measurements \mathbf{r} of the form

$$\mathbf{r} = \mathbf{x}^0 + \mathbf{e}, \quad \mathbf{e} \sim \mathcal{N}(\mathbf{0}, \nu \mathbf{I}), \quad (10)$$

for some variance $\nu > 0$.

Image denoising has been studied for decades (see, e.g., the overviews [2], [3]), with the result that high performance methods are now readily available. Today’s state-of-the-art denoisers include those based on image-dependent filtering algorithms (e.g., BM3D [5]) or deep neural networks (e.g., TNRD [6], DnCNN [7]). Importantly, many denoisers are not variational in nature, i.e., they do not declare an explicit regularizer $\lambda\rho(\mathbf{x})$.

Leveraging the denoising interpretation of ADMM, Venkatakrishnan, Bouman, and Wolberg [9] proposed to replace line 3 of Algorithm 1 with a call to a sophisticated image denoiser, such as BM3D, and dubbed their approach *Plug-and-Play* (PnP) ADMM. Numerical experiments show that PnP-ADMM works very well in most cases. However, when the denoiser used in PnP-ADMM comes with no explicit regularization $\rho(\mathbf{x})$, it is not clear what objective PnP-ADMM is minimizing and PnP-ADMM convergence is difficult to characterize.

Shortly thereafter, a related approach was proposed based on the approximate message passing (AMP) algorithm [12], called Denoising-based AMP (D-AMP) [13]. D-AMP exploits the fact that, for large i.i.d. random \mathbf{A} , some internal AMP variables naturally obey (10) and are thus amenable to denoising. An extension called D-VAMP that covers the wider class of “right rotationally invariant” random matrices was then proposed in [14]. Rigorous analyses of D-AMP and D-VAMP were recently published in [15] and [16], respectively.

D. Regularization by Denoising (RED)

As briefly discussed in the Introduction, Romano, Elad, and Milanfar [1] proposed a radically new way to exploit an image denoiser, which they call *regularization by denoising* (RED). Given an arbitrary image denoiser $\mathbf{f} : \mathbb{R}^N \rightarrow \mathbb{R}^N$, they proposed to construct an explicit regularizer of the form

$$\rho_{\text{red}}(\mathbf{x}) \triangleq \frac{1}{2} \mathbf{x}^\top (\mathbf{x} - \mathbf{f}(\mathbf{x})) \quad (11)$$

to use within the variational framework (2). The advantage of using an explicit regularizer is that a wide variety of

optimization algorithms can be used to solve (2) and their convergence can be tractably analyzed.

In [1], numerical evidence is presented to show that image denoisers $\mathbf{f}(\cdot)$ are *locally homogeneous* (LH), i.e.,

$$(1 + \epsilon)\mathbf{f}(\mathbf{x}) = \mathbf{f}((1 + \epsilon)\mathbf{x}) \quad \forall \mathbf{x} \quad (12)$$

for sufficiently small $\epsilon \in \mathbb{R} \setminus 0$. For such denoisers, Romano et al. claim [1, Eq.(28)] that $\rho_{\text{red}}(\cdot)$ obeys the gradient rule

$$\nabla \rho_{\text{red}}(\mathbf{x}) = \mathbf{x} - \mathbf{f}(\mathbf{x}). \quad (13)$$

If $\nabla \rho_{\text{red}}(\mathbf{x}) = \mathbf{x} - \mathbf{f}(\mathbf{x})$, then any minimizer $\hat{\mathbf{x}}$ of the variational objective under quadratic loss,

$$\frac{1}{2\sigma^2} \|\mathbf{A}\mathbf{x} - \mathbf{y}\|^2 + \lambda \rho_{\text{red}}(\mathbf{x}) \triangleq C_{\text{red}}(\mathbf{x}), \quad (14)$$

must yield $\nabla C_{\text{red}}(\hat{\mathbf{x}}) = \mathbf{0}$, i.e., must obey

$$\mathbf{0} = \frac{1}{\sigma^2} \mathbf{A}^\top (\mathbf{A}\hat{\mathbf{x}} - \mathbf{y}) + \lambda(\hat{\mathbf{x}} - \mathbf{f}(\hat{\mathbf{x}})). \quad (15)$$

Based on this line of reasoning, Romano et al. proposed several iterative algorithms that find an $\hat{\mathbf{x}}$ satisfying the fixed-point condition (15), which we will refer to as “RED algorithms.”

III. CLARIFICATIONS ON RED

In this section, we first show that the gradient expression (13) holds if and only if the denoiser $\mathbf{f}(\cdot)$ is LH and has Jacobian symmetry (JS). We then establish that many popular denoisers lack JS, such as the median filter (MF) [17], non-local means (NLM) [4], BM3D [5], TNRD [6], and DnCNN [7]. For such denoisers, the RED algorithms cannot be explained by $\rho_{\text{red}}(\cdot)$ in (11). We also show a more general result: when a denoiser lacks JS, there exists no regularizer $\rho(\cdot)$ whose gradient expression matches (13). Thus, the problem is not the specific form of $\rho_{\text{red}}(\cdot)$ in (11) but rather the broader pursuit of explicit regularization.

A. Preliminaries

We first state some definitions and assumptions. In the sequel, we denote the i th component of $\mathbf{f}(\mathbf{x})$ by $f_i(\mathbf{x})$, the gradient of $f_i(\cdot)$ at \mathbf{x} by

$$\nabla f_i(\mathbf{x}) \triangleq \left[\frac{\partial f_i(\mathbf{x})}{\partial x_1} \dots \frac{\partial f_i(\mathbf{x})}{\partial x_N} \right]^\top, \quad (16)$$

and the Jacobian of $\mathbf{f}(\cdot)$ at \mathbf{x} by

$$J\mathbf{f}(\mathbf{x}) \triangleq \begin{bmatrix} \frac{\partial f_1(\mathbf{x})}{\partial x_1} & \frac{\partial f_1(\mathbf{x})}{\partial x_2} & \dots & \frac{\partial f_1(\mathbf{x})}{\partial x_N} \\ \frac{\partial f_2(\mathbf{x})}{\partial x_1} & \frac{\partial f_2(\mathbf{x})}{\partial x_2} & \dots & \frac{\partial f_2(\mathbf{x})}{\partial x_N} \\ \vdots & \vdots & \ddots & \vdots \\ \frac{\partial f_N(\mathbf{x})}{\partial x_1} & \frac{\partial f_N(\mathbf{x})}{\partial x_2} & \dots & \frac{\partial f_N(\mathbf{x})}{\partial x_N} \end{bmatrix}. \quad (17)$$

Without loss of generality, we take $[0, 255]^N \subset \mathbb{R}^N$ to be the set of possible images. A given denoiser $\mathbf{f}(\cdot)$ may involve decision boundaries $\mathcal{D} \subset [0, 255]^N$ at which its behavior changes suddenly. We assume that these boundaries are a closed set of measure zero and work instead with the open set $\mathcal{X} \triangleq (0, 255)^N \setminus \mathcal{D}$, which contains almost all images.

We furthermore assume that $\mathbf{f} : \mathbb{R}^N \rightarrow \mathbb{R}^N$ is *differentiable* on \mathcal{X} , which means [18, p.212] that, for any $\mathbf{x} \in \mathcal{X}$, there exists a matrix $\mathbf{J} \in \mathbb{R}^{N \times N}$ for which

$$\lim_{\mathbf{w} \rightarrow 0} \frac{\|\mathbf{f}(\mathbf{x} + \mathbf{w}) - \mathbf{f}(\mathbf{x}) - \mathbf{J}\mathbf{w}\|}{\|\mathbf{w}\|} = 0. \quad (18)$$

When \mathbf{J} exists, it can be shown [18, p.216] that $\mathbf{J} = J\mathbf{f}(\mathbf{x})$.

B. The RED Gradient

We first recall a result that was established in [1].

Lemma 1 (Local homogeneity [1]). *Suppose that denoiser $\mathbf{f}(\cdot)$ is locally homogeneous. Then $[J\mathbf{f}(\mathbf{x})]\mathbf{x} = \mathbf{f}(\mathbf{x})$.*

Proof. Our proof is based on differentiability and avoids the need to define a directional derivative. From (18), we have

$$0 = \lim_{\epsilon \rightarrow 0} \frac{\|\mathbf{f}(\mathbf{x} + \epsilon\mathbf{x}) - \mathbf{f}(\mathbf{x}) - [J\mathbf{f}(\mathbf{x})]\mathbf{x}\epsilon\|}{\|\epsilon\mathbf{x}\|} \quad \forall \mathbf{x} \in \mathcal{X} \quad (19)$$

$$= \lim_{\epsilon \rightarrow 0} \frac{\|(1 + \epsilon)\mathbf{f}(\mathbf{x}) - \mathbf{f}(\mathbf{x}) - [J\mathbf{f}(\mathbf{x})]\mathbf{x}\epsilon\|}{\|\epsilon\mathbf{x}\|} \quad \forall \mathbf{x} \in \mathcal{X} \quad (20)$$

$$= \lim_{\epsilon \rightarrow 0} \frac{\|\mathbf{f}(\mathbf{x}) - [J\mathbf{f}(\mathbf{x})]\mathbf{x}\|}{\|\mathbf{x}\|} \quad \forall \mathbf{x} \in \mathcal{X}, \quad (21)$$

where (20) follows from local homogeneity (12). Equation (21) implies that $[J\mathbf{f}(\mathbf{x})]\mathbf{x} = \mathbf{f}(\mathbf{x}) \quad \forall \mathbf{x} \in \mathcal{X}$. \square

We now state one of the main results of this section.

Lemma 2 (RED gradient). *For $\rho_{\text{red}}(\cdot)$ defined in (11),*

$$\nabla \rho_{\text{red}}(\mathbf{x}) = \mathbf{x} - \frac{1}{2}\mathbf{f}(\mathbf{x}) - \frac{1}{2}[J\mathbf{f}(\mathbf{x})]^\top \mathbf{x}. \quad (22)$$

Proof. For any $\mathbf{x} \in \mathcal{X}$ and $n = 1, \dots, N$,

$$\frac{\partial \rho_{\text{red}}(\mathbf{x})}{\partial x_n} = \frac{\partial}{\partial x_n} \frac{1}{2} \sum_{i=1}^N (x_i^2 - x_i f_i(\mathbf{x})) \quad (23)$$

$$= \frac{1}{2} \frac{\partial}{\partial x_n} \left(x_n^2 - x_n f_n(\mathbf{x}) + \sum_{i \neq n} x_i^2 - \sum_{i \neq n} x_i f_i(\mathbf{x}) \right) \quad (24)$$

$$= \frac{1}{2} \left(2x_n - f_n(\mathbf{x}) - x_n \frac{\partial f_n(\mathbf{x})}{\partial x_n} - \sum_{i \neq n} x_i \frac{\partial f_i(\mathbf{x})}{\partial x_n} \right) \quad (25)$$

$$= x_n - \frac{1}{2} f_n(\mathbf{x}) - \frac{1}{2} \sum_{i=1}^N x_i \frac{\partial f_i(\mathbf{x})}{\partial x_n} \quad (26)$$

$$= x_n - \frac{1}{2} f_n(\mathbf{x}) - \frac{1}{2} [[J\mathbf{f}(\mathbf{x})]^\top \mathbf{x}]_n, \quad (27)$$

using the definition of $J\mathbf{f}(\mathbf{x})$ from (17). Collecting $\{\frac{\partial \rho_{\text{red}}(\mathbf{x})}{\partial x_n}\}_{n=1}^N$ into the gradient vector (13) yields (22). \square

Note that the gradient expression (22) differs from (13).

Lemma 3 (Clarification on (13)). *Suppose that the denoiser $\mathbf{f}(\cdot)$ is locally homogeneous. Then the RED gradient expression (13) holds if and only if $J\mathbf{f}(\mathbf{x}) = [J\mathbf{f}(\mathbf{x})]^\top$.*

Proof. If $J\mathbf{f}(\mathbf{x}) = [J\mathbf{f}(\mathbf{x})]^\top$, then the last term in (22) becomes $-\frac{1}{2}[J\mathbf{f}(\mathbf{x})]\mathbf{x}$, which equals $-\frac{1}{2}\mathbf{f}(\mathbf{x})$ by Lemma 1, in which case (22) agrees with (13). But if $J\mathbf{f}(\mathbf{x}) \neq [J\mathbf{f}(\mathbf{x})]^\top$, then (22) differs from (13). \square

C. Impossibility of Explicit Regularization

For denoisers $f(\cdot)$ that lack Jacobian symmetry (JS), Lemma 3 establishes that the gradient expression (13) does not hold. Yet (13) leads to the fixed-point condition (15) on which all RED algorithms in [1] are based. The fact that these algorithms work well in practice suggests that “ $\nabla\rho(\mathbf{x}) = \mathbf{x} - f(\mathbf{x})$ ” is a desirable property for a regularizer $\rho(\mathbf{x})$ to have. But the regularization $\rho_{\text{red}}(\mathbf{x})$ in (11) does not lead to this property when $f(\cdot)$ lacks JS. Thus an important question is:

Does there exist some other regularization $\rho(\cdot)$ for which $\nabla\rho(\mathbf{x}) = \mathbf{x} - f(\mathbf{x})$ when $f(\cdot)$ is non-JS?

The following theorem provides the answer.

Theorem 1 (Impossibility). *Suppose that denoiser $f(\cdot)$ has a non-symmetric Jacobian. Then there exists no regularization $\rho(\cdot)$ for which $\nabla\rho(\mathbf{x}) = \mathbf{x} - f(\mathbf{x})$.*

Proof. To prove the theorem, we view $f : \mathcal{X} \rightarrow \mathbb{R}^N$ as a vector field. Theorem 4.3.8 in [19] says that a vector field f is *conservative* if and only if there exists a continuously differentiable potential $\bar{\rho} : \mathcal{X} \rightarrow \mathbb{R}$ for which $\nabla\bar{\rho} = f$. Furthermore, Theorem 4.3.10 in [19] says that if f is conservative, then the Jacobian Jf is symmetric. Thus, by the contrapositive, if the Jacobian Jf is *not* symmetric, then no such potential $\bar{\rho}$ exists.

To apply this result to our problem, we define

$$\rho(\mathbf{x}) \triangleq \frac{1}{2}\|\mathbf{x}\|^2 - \bar{\rho}(\mathbf{x}) \quad (28)$$

and notice that

$$\nabla\rho(\mathbf{x}) = \mathbf{x} - \nabla\bar{\rho}(\mathbf{x}) = \mathbf{x} - f(\mathbf{x}). \quad (29)$$

Thus, if $Jf(\mathbf{x})$ is non-symmetric, then $J[\mathbf{x} - f(\mathbf{x})] = \mathbf{I} - Jf(\mathbf{x})$ is non-symmetric, which means that there exists no ρ for which (29) holds. \square

Thus, the problem is not the specific form of $\rho_{\text{red}}(\cdot)$ in (11) but rather the broader pursuit of “regularization by denoising.”

D. Analysis of Jacobian Symmetry

The previous sections motivate an important question: Do commonly-used image denoisers have sufficient JS?

For some denoisers, JS can be studied analytically. For example, consider the “transform domain thresholding” (TDT) denoisers of the form

$$f(\mathbf{x}) \triangleq \mathbf{W}^\top \mathbf{g}(\mathbf{W}\mathbf{x}), \quad (30)$$

where $\mathbf{g}(\cdot)$ performs componentwise (e.g., soft or hard) thresholding and \mathbf{W} is some transform, as occurs in the context of wavelet shrinkage [20], with or without cycle-spinning [21]. Using $g'_n(\cdot)$ to denote the derivative of $g_n(\cdot)$, we have

$$\frac{\partial f_n(\mathbf{x})}{\partial x_q} = \sum_{i=1}^N w_{in} g'_i \left(\sum_{j=1}^N w_{ij} x_j \right) w_{iq} = \frac{\partial f_q(\mathbf{x})}{\partial x_n}, \quad (31)$$

and so the Jacobian of $f(\cdot)$ is perfectly symmetric.

Another class of denoisers with perfectly symmetric Jacobians are those that produce MAP or MMSE optimal $\hat{\mathbf{x}}$ under some assumed prior $\hat{p}_{\mathbf{x}}$. In the MAP case, $\hat{\mathbf{x}}$ minimizes (over

\mathbf{x}) the cost $c(\mathbf{x}; \mathbf{r}) = \frac{1}{2\nu}\|\mathbf{x} - \mathbf{r}\|^2 - \ln \hat{p}_{\mathbf{x}}(\mathbf{x})$ for noisy input \mathbf{r} . If we define $\phi(\mathbf{r}) \triangleq \min_{\mathbf{x}} c(\mathbf{x}; \mathbf{r})$, known as the Moreau-Yosida envelope of $-\ln \hat{p}_{\mathbf{x}}$, then $\hat{\mathbf{x}} = f(\mathbf{r}) = \mathbf{r} - \nu \nabla \phi(\mathbf{r})$, as discussed in [22]. The elements in the Jacobian are therefore $[Jf(\mathbf{r})]_{n,q} = \frac{\partial f_n(\mathbf{r})}{\partial r_q} = \delta_{n-q} - \nu \frac{\partial^2 \phi(\mathbf{r})}{\partial r_q \partial r_n}$, and so the Jacobian matrix is symmetric. In the MMSE case, we have that $f(\mathbf{r}) = \mathbf{r} - \nabla \rho_{\text{LL}}(\mathbf{r})$ for $\rho_{\text{LL}}(\cdot)$ defined in (51) (see Lemma 4), and so $[Jf(\mathbf{r})]_{n,q} = \delta_{n-q} - \frac{\partial^2 \rho_{\text{LL}}(\mathbf{r})}{\partial r_q \partial r_n}$, again implying that the Jacobian is symmetric. But it is difficult to say anything about the Jacobian symmetry of *approximate* MAP or MMSE denoisers.

Now let us consider the more general class of denoisers

$$f(\mathbf{x}) = \mathbf{W}(\mathbf{x})\mathbf{x}, \quad (32)$$

sometimes called “pseudo-linear” [3]. For simplicity, we assume that $\mathbf{W}(\cdot)$ is differentiable on \mathcal{X} . In this case, using the chain rule, we have

$$\frac{\partial f_n(\mathbf{x})}{\partial x_q} = w_{nq}(\mathbf{x}) + \sum_{i=1}^N \frac{\partial w_{ni}(\mathbf{x})}{\partial x_q} x_i, \quad (33)$$

and so the Jacobian is symmetric for all $\mathbf{x} \in \mathcal{X}$ whenever

- 1) $\mathbf{W}(\mathbf{x})$ is symmetric $\forall \mathbf{x} \in \mathcal{X}$,
- 2) $\sum_{i=1}^N \frac{\partial w_{ni}(\mathbf{x})}{\partial x_q} x_i = \sum_{i=1}^N \frac{\partial w_{qi}(\mathbf{x})}{\partial x_n} x_i \quad \forall \mathbf{x} \in \mathcal{X}$.

When \mathbf{W} is \mathbf{x} -invariant (i.e., $f(\cdot)$ is linear) and symmetric, both of these conditions are satisfied. This latter case was exploited for RED in [23]. The case of non-linear $\mathbf{W}(\cdot)$ is more complicated. Although $\mathbf{W}(\cdot)$ can be symmetrized (see [24], [25]), it is not clear whether the second condition will be satisfied.

E. Jacobian Symmetry Experiments

For denoisers that do not admit a tractable analysis, we can still evaluate the Jacobian of $f(\cdot)$ at \mathbf{x} numerically via

$$\frac{f_i(\mathbf{x} + \epsilon \mathbf{e}_n) - f_i(\mathbf{x} - \epsilon \mathbf{e}_n)}{2\epsilon} \triangleq [\widehat{Jf}(\mathbf{x})]_{i,n}, \quad (34)$$

where \mathbf{e}_n denotes the n th column of \mathbf{I}_N and $\epsilon > 0$ is small ($\epsilon = 1 \times 10^{-3}$ in our experiments). For the purpose of quantifying JS, we define the normalized error metric

$$e_f^J(\mathbf{x}) \triangleq \frac{\|\widehat{Jf}(\mathbf{x}) - [\widehat{Jf}(\mathbf{x})]^\top\|_F^2}{\|\widehat{Jf}(\mathbf{x})\|_F^2}, \quad (35)$$

which should be nearly zero for a symmetric Jacobian.

Table I shows the average value of $e_f^J(\mathbf{x})$ for 16 different image patches¹ of size 16×16 , using denoisers that assumed a noise variance of 3.25². The denoisers tested were the TDT from (30) with the 2D Haar wavelet transform and soft-thresholding, the median filter (MF) [17] with a 3×3 window, non-local means (NLM) [4], BM3D [5], TNRD [6], and DnCNN [7]. Table I shows that the Jacobians of all but the TDT denoiser are far from symmetric.

Jacobian symmetry is a somewhat abstract construct; what we really care about is the accuracy of the RED gradient

¹We used the center patches of the standard Barbara, Bike, Boats, Butterfly, Cameraman, Flower, Hat, House, Leaves, Lena, Parrots, Parthenon, Peppers, Plants, Raccoon, and Starfish test images, all of size 256×256 .

	TDT	MF	NLM	BM3D	TNRD	DnCNN
$e_f^J(\mathbf{x})$	4.11e-21	1.35	0.118	0.186	0.0151	0.194

TABLE I
AVERAGE JACOBIAN-SYMMETRY ERROR ON 16×16 IMAGES

$e_f^J(\mathbf{x})$	TDT	MF	NLM	BM3D	TNRD	DnCNN
$\nabla \rho_{\text{red}}(\mathbf{x})$ from (13)	0.565	0.966	0.913	1.00	0.957	0.852
$\nabla \rho_{\text{red}}(\mathbf{x})$ from (38)	0.565	6.09e-15	0.0699	0.344	0.139	1.20
$\nabla \rho_{\text{red}}(\mathbf{x})$ from (22)	3.39e-19	2.65e-15	6.17e-21	2.14e-13	5.42e-17	1.02e-12

TABLE II
AVERAGE GRADIENT ERROR ON 16×16 IMAGES

expressions (13) and (22). To assess gradient accuracy, we numerically evaluated the gradient of $\rho_{\text{red}}(\cdot)$ at \mathbf{x} using

$$\frac{\rho_{\text{red}}(\mathbf{x} + \epsilon \mathbf{e}_n) - \rho_{\text{red}}(\mathbf{x} - \epsilon \mathbf{e}_n)}{2\epsilon} \triangleq \widehat{[\nabla \rho_{\text{red}}(\mathbf{x})]}_n \quad (36)$$

and compared the result to the analytical expressions (13) and (22). Table II reports the normalized gradient error

$$e_f^{\nabla}(\mathbf{x}) \triangleq \frac{\|\nabla \rho_{\text{red}}(\mathbf{x}) - \widehat{\nabla \rho_{\text{red}}(\mathbf{x})}\|^2}{\|\widehat{\nabla \rho_{\text{red}}(\mathbf{x})}\|^2} \quad (37)$$

for the same ϵ , images, and denoisers used in Table I. The results in Table II show that, for all tested denoisers, the numerical gradient $\widehat{\nabla \rho_{\text{red}}(\cdot)}$ closely matches the analytical expression for $\nabla \rho_{\text{red}}(\cdot)$ from (22), but not that from (13). The mismatch between $\widehat{\nabla \rho_{\text{red}}(\cdot)}$ and $\nabla \rho_{\text{red}}(\cdot)$ from (13) is partly due to insufficient JS and partly due to insufficient LH, as we establish below.

F. Local Homogeneity Experiments

Recall that the TDT denoiser has a symmetric Jacobian, both theoretically and empirically. Yet Table II reports a disagreement between the $\nabla \rho_{\text{red}}(\cdot)$ expressions (13) and (22) for TDT. We now show that this disagreement is due to insufficient local homogeneity (LH).

To do this, we introduce yet another RED gradient expression,

$$\nabla \rho_{\text{red}}(\mathbf{x}) \stackrel{\text{LH}}{=} \mathbf{x} - \frac{1}{2}[\mathbf{J}\mathbf{f}(\mathbf{x})]\mathbf{x} - \frac{1}{2}[\mathbf{J}\mathbf{f}(\mathbf{x})]^{\top} \mathbf{x}, \quad (38)$$

which results from combining (22) with Lemma 1. Here, $\stackrel{\text{LH}}{=}$ indicates that (38) holds under LH. In contrast, the gradient expression (13) holds under both LH and Jacobian symmetry, while the gradient expression (22) holds in general (i.e., even in the absence of LH and/or Jacobian symmetry). We also introduce two normalized error metrics for LH,

$$e_f^{\text{LH},1}(\mathbf{x}) \triangleq \frac{\|\mathbf{f}((1 + \epsilon)\mathbf{x}) - (1 + \epsilon)\mathbf{f}(\mathbf{x})\|^2}{\|(1 + \epsilon)\mathbf{f}(\mathbf{x})\|^2} \quad (39)$$

$$e_f^{\text{LH},2}(\mathbf{x}) \triangleq \frac{\|[\widehat{\mathbf{J}}\mathbf{f}(\mathbf{x})]\mathbf{x} - \mathbf{f}(\mathbf{x})\|^2}{\|\mathbf{f}(\mathbf{x})\|^2}. \quad (40)$$

which should both be nearly zero for LH $\mathbf{f}(\cdot)$. Note that $e_f^{\text{LH},1}$ quantifies LH according to definition (12) and closely matches the numerical analysis of LH in [1]. Meanwhile, $e_f^{\text{LH},2}$ quantifies LH according to Lemma 1 and to how LH is used in the gradient expressions (13) and (38).

	TDT	MF	NLM	BM3D	TNRD	DnCNN
$e_f^{\text{LH},1}(\mathbf{x})$	7.99e-10	0	5.60e-9	1.52e-13	5.09e-10	2.06e-9
$e_f^{\text{LH},2}(\mathbf{x})$	4.10e-4	2.14e-15	5.63e-3	0.214	2.60e-4	8.02e-3

TABLE III
AVERAGE LOCAL-HOMOGENEITY ERROR ON 16×16 IMAGES

The middle row of Table II reports the average gradient error of the gradient expression (38), and Table III reports average LH error for the metrics $e_f^{\text{LH},1}$ and $e_f^{\text{LH},2}$. There we see that the average $e_f^{\text{LH},1}$ error is small for all denoisers, consistent with the experiments in [1]. But the average $e_f^{\text{LH},2}$ error is several orders of magnitude larger (for all but the MF denoiser). As discussed below, these seemingly small imperfections in LH have a significant effect on the RED gradient expressions (13) and (38).

Starting with the TDT denoiser, Table II shows that the gradient error on (38) is large, which can only be caused by insufficient LH. The insufficient LH is confirmed in Table III, which shows that the value of $e_f^{\text{LH},2}(\mathbf{x})$ for TDT is non-negligible, especially in comparison to the value for MF.

Continuing with the MF denoiser, Table I indicates that its Jacobian is far from symmetric, while Table III indicates that it is LH. The gradient results in Table II are consistent with these behaviors: the $\nabla \rho_{\text{red}}(\mathbf{x})$ expression (38) is accurate on account of LH being satisfied, but the $\nabla \rho_{\text{red}}(\mathbf{x})$ expression (13) is inaccurate on account of a lack in JS.

The results for the remaining denoisers NLM, BM3D, TNRD, and BM3D show a common trend: they have non-trivial levels of *both* JS error (see Table I) and LH error (see Table III). As a result, the gradient expressions (13) and (38) are *both* inaccurate (see Table II).

In conclusion, the experiments in this section show that the RED gradient expressions (13) and (38) are very sensitive to small imperfections in LH. Although the experiments in [1] suggested that many popular image denoisers are approximately LH, our experiments suggest that their levels of LH are insufficient to maintain the accuracy of the RED gradient expressions (13) and (38).

G. Example RED-SD Trajectory

We now provide an example of how the RED algorithms from [1] do not necessarily minimize the variational objective $\ell(\mathbf{x}; \mathbf{y}) + \lambda \rho_{\text{red}}(\mathbf{x})$.

Figure 1 plots the RED Cost $C_{\text{red}}(\mathbf{x}_k)$ from (14) and the error on the fixed-point condition (15), i.e.,

$$\|\mathbf{A}^{\top}(\mathbf{A}\mathbf{x}_k - \mathbf{y})/\sigma^2 + \lambda(\mathbf{x}_k - \mathbf{f}(\mathbf{x}_k))\|^2,$$

versus iteration k for a trajectory $\{\mathbf{x}_k\}_{k=1}^K$ produced by the steepest-descent (SD) RED algorithm from [1]. For this experiment, we used the 3×3 median-filter for $\mathbf{f}(\cdot)$, the Starfish image, and noisy measurements $\mathbf{y} = \mathbf{x} + \mathcal{N}(\mathbf{0}, \sigma^2 \mathbf{I})$ with $\sigma^2 = 20$ (i.e., $\mathbf{A} = \mathbf{I}$ in (1)).

Figure 1 shows that, although the RED-SD algorithm asymptotically satisfies the fixed-point condition (15), the RED cost function $C_{\text{red}}(\mathbf{x}_k)$ does not decrease with k , as would be expected if the RED algorithms truly minimize the RED cost $C_{\text{red}}(\cdot)$. This behavior implies that any optimization

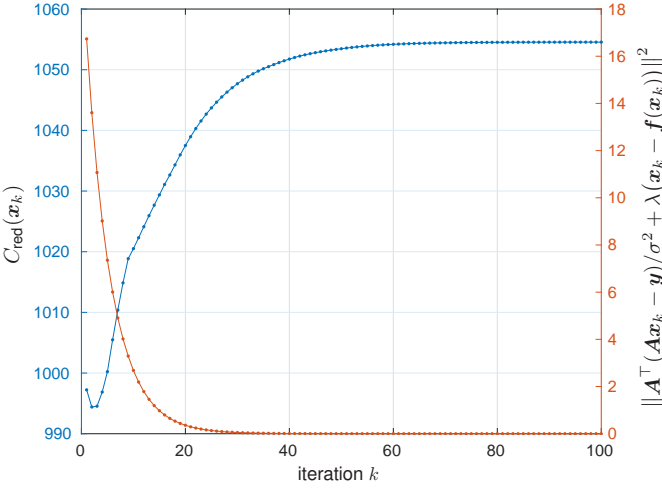


Fig. 1. RED cost $C_{\text{red}}(\mathbf{x}_k)$ and fixed-point error $\|\mathbf{A}^\top(\mathbf{A}\mathbf{x}_k - \mathbf{y})/\sigma^2 + (\mathbf{x}_k - \mathbf{f}(\mathbf{x}_k))\|^2$ versus iteration k for $\{\mathbf{x}_k\}_{k=1}^K$ produced by the RED-SD algorithm from [1]. Although the fixed-point condition is asymptotically satisfied, the RED cost does not decrease with k .

algorithm that monitors the objective value $C_{\text{red}}(\mathbf{x}_k)$ for, say, backtracking line-search (e.g., the FASTA algorithm [26]), cannot be applied in the context of RED.

H. Hessian and Convexity

From (26), the (n, j) th element of the Hessian of $\rho_{\text{red}}(\mathbf{x})$ equals

$$\frac{\partial^2 \rho_{\text{red}}(\mathbf{x})}{\partial x_n \partial x_j} = \frac{\partial}{\partial x_j} \left(x_n - \frac{1}{2} f_n(\mathbf{x}) - \frac{1}{2} \sum_{i=1}^N x_i \frac{\partial f_i(\mathbf{x})}{\partial x_n} \right) \quad (41)$$

$$\begin{aligned} &= \delta_{n-j} - \frac{1}{2} \frac{\partial f_n(\mathbf{x})}{\partial x_j} - \frac{1}{2} \frac{\partial f_j(\mathbf{x})}{\partial x_n} - \frac{1}{2} x_j \frac{\partial^2 f_j(\mathbf{x})}{\partial x_n \partial x_j} \\ &\quad - \frac{1}{2} \sum_{i \neq j} x_i \frac{\partial^2 f_i(\mathbf{x})}{\partial x_n \partial x_j} \end{aligned} \quad (42)$$

$$= \delta_{n-j} - \frac{1}{2} \frac{\partial f_n(\mathbf{x})}{\partial x_j} - \frac{1}{2} \frac{\partial f_j(\mathbf{x})}{\partial x_n} - \frac{1}{2} \sum_{i=1}^N x_i \frac{\partial^2 f_i(\mathbf{x})}{\partial x_n \partial x_j}. \quad (43)$$

where $\delta_k = 1$ if $k = 0$ and otherwise $\delta_k = 0$. Thus, the Hessian of $\rho_{\text{red}}(\cdot)$ at \mathbf{x} equals

$$H\rho_{\text{red}}(\mathbf{x}) = \mathbf{I} - \frac{1}{2} J\mathbf{f}(\mathbf{x}) - \frac{1}{2} [J\mathbf{f}(\mathbf{x})]^\top - \frac{1}{2} \sum_{i=1}^N x_i Hf_i(\mathbf{x}). \quad (44)$$

This expression can be contrasted with the Hessian expression from [1, (60)], which reads

$$\mathbf{I} - J\mathbf{f}(\mathbf{x}). \quad (45)$$

Interestingly, (44) differs from (45) even when the denoiser has a symmetric Jacobian $J\mathbf{f}(\mathbf{x})$. One implication is that, even if eigenvalues of $J\mathbf{f}(\mathbf{x})$ are limited to the interval $[0, 1]$, the Hessian $H\rho_{\text{red}}(\mathbf{x})$ may not be positive semi-definite due to the last term in (44), with negative implications on the convexity of $\rho_{\text{red}}(\cdot)$. That said, the RED algorithms do not

actually minimize the variational objective $\ell(\mathbf{x}; \mathbf{y}) + \lambda \rho_{\text{red}}(\mathbf{x})$ for common denoisers $\mathbf{f}(\cdot)$ (as established in Section III-G), and so the convexity of $\rho_{\text{red}}(\cdot)$ may not matter in practice.

IV. SCORE-MATCHING BY DENOISING

As discussed in Section II-D, the RED algorithms proposed in [1] are explicitly based on gradient rule

$$\nabla \rho(\mathbf{x}) = \mathbf{x} - \mathbf{f}(\mathbf{x}). \quad (46)$$

This rule appears to be useful, since these algorithms work very well in practice. But Section III established that $\rho_{\text{red}}(\cdot)$ from (11) does not usually satisfy (46). We are thus motivated to seek an alternative explanation for the RED algorithms. In this section, we explain them through a framework that we call “score-matching by denoising” (SMD).

A. Regularization by Log-Likelihood

As a precursor to the SMD framework, we first propose a technique called regularization by log-likelihood.

Recall the measurement model (10) used to define the “denoising” problem, repeated in (47) for convenience:

$$\mathbf{r} = \mathbf{x}^0 + \mathbf{e}, \quad \mathbf{e} \sim \mathcal{N}(\mathbf{0}, \nu \mathbf{I}). \quad (47)$$

To avoid confusion, we will refer to \mathbf{r} as “pseudo-measurements” and \mathbf{y} as “measurements.” From (47), the likelihood function for the pseudo-measurements is $p(\mathbf{r}|\mathbf{x}; \nu) = \mathcal{N}(\mathbf{r}; \mathbf{x}, \nu \mathbf{I})$.

Now, suppose that we model the true image \mathbf{x}^0 as a realization of a random vector \mathbf{x} with prior pdf $\hat{p}_x(\mathbf{x})$. We write “ \hat{p}_x ” to emphasize that the model distribution may differ from the true distribution p_x (from which the image \mathbf{x} is actually drawn). Under this prior model, the MMSE denoiser of \mathbf{x} from \mathbf{r} is

$$\hat{\mathbf{f}}_{\text{mmse}, \nu}(\mathbf{r}) \triangleq \mathbb{E}_{\hat{p}_x} \{ \mathbf{x} | \mathbf{r} = \mathbf{x} + \mathcal{N}(\mathbf{0}, \nu \mathbf{I}) \}, \quad (48)$$

and the likelihood of observing \mathbf{r} is

$$\hat{p}_r(\mathbf{r}; \nu) \triangleq \int_{\mathbb{R}^N} p(\mathbf{r}|\mathbf{x}; \nu) \hat{p}_x(\mathbf{x}) d\mathbf{x} \quad (49)$$

$$= \int_{\mathbb{R}^N} \mathcal{N}(\mathbf{r}; \mathbf{x}, \nu \mathbf{I}) \hat{p}_x(\mathbf{x}) d\mathbf{x}. \quad (50)$$

In what we will refer to as *regularization by log-likelihood* (RLL), an explicit regularizer is constructed with the form

$$\rho_{\text{LL}}(\mathbf{r}; \nu) \triangleq -\nu \ln \hat{p}_r(\mathbf{r}; \nu). \quad (51)$$

As we now show, $\rho_{\text{LL}}(\cdot)$ has the desired property (46).

Lemma 4. (RLL) For $\rho_{\text{LL}}(\mathbf{r}; \nu)$ defined in (51),

$$\nabla \rho_{\text{LL}}(\mathbf{r}; \nu) = \mathbf{r} - \hat{\mathbf{f}}_{\text{mmse}, \nu}(\mathbf{r}), \quad (52)$$

where $\hat{\mathbf{f}}_{\text{mmse}, \nu}(\cdot)$ is the MMSE denoiser from (48).

Proof. Equation (52) is a direct consequence of a classical result known as Tweedie's formula [27], [28]. A short proof, from first principles, is now given for completeness.

$$\frac{\partial}{\partial r_n} \rho_{\text{LL}}(\mathbf{r}; \nu) = -\nu \frac{\partial}{\partial r_n} \ln \int_{\mathbb{R}^N} \widehat{p}_{\mathbf{x}}(\mathbf{x}) \mathcal{N}(\mathbf{r}; \mathbf{x}, \nu \mathbf{I}) d\mathbf{x} \quad (53)$$

$$= -\frac{\nu \int_{\mathbb{R}^N} \widehat{p}_{\mathbf{x}}(\mathbf{x}) \frac{\partial}{\partial r_n} \mathcal{N}(\mathbf{r}; \mathbf{x}, \nu \mathbf{I}) d\mathbf{x}}{\int_{\mathbb{R}^N} \widehat{p}_{\mathbf{x}}(\mathbf{x}) \mathcal{N}(\mathbf{r}; \mathbf{x}, \nu \mathbf{I}) d\mathbf{x}} \quad (54)$$

$$= \frac{\int_{\mathbb{R}^N} \widehat{p}_{\mathbf{x}}(\mathbf{x}) \mathcal{N}(\mathbf{r}; \mathbf{x}, \nu \mathbf{I}) (r_n - x_n) d\mathbf{x}}{\int_{\mathbb{R}^N} \widehat{p}_{\mathbf{x}}(\mathbf{x}) \mathcal{N}(\mathbf{r}; \mathbf{x}, \nu \mathbf{I}) d\mathbf{x}} \quad (55)$$

$$= r_n - \int_{\mathbb{R}^N} x_n \frac{\widehat{p}_{\mathbf{x}}(\mathbf{x}) \mathcal{N}(\mathbf{r}; \mathbf{x}, \nu \mathbf{I})}{\int_{\mathbb{R}^N} \widehat{p}_{\mathbf{x}}(\mathbf{x}') \mathcal{N}(\mathbf{r}; \mathbf{x}', \nu \mathbf{I}) d\mathbf{x}'} d\mathbf{x}' \quad (56)$$

$$= r_n - \int_{\mathbb{R}^N} x_n \widehat{p}_{\mathbf{x}|\mathbf{r}}(\mathbf{x}|\mathbf{r}; \nu) d\mathbf{x} \quad (57)$$

$$= r_n - [\widehat{\mathbf{f}}_{\text{mmse}, \nu}(\mathbf{r})]_n, \quad (58)$$

where (55) used $\frac{\partial}{\partial r_n} \mathcal{N}(\mathbf{r}; \mathbf{x}, \nu \mathbf{I}) = \mathcal{N}(\mathbf{r}; \mathbf{x}, \nu \mathbf{I})(x_n - r_n)/\nu$. Stacking (58) for $n = 1, \dots, N$ in a vector yields (52). \square

Thus, if the RLL regularizer $\rho_{\text{LL}}(\cdot; \nu)$ is used in the optimization problem (14), then the solution $\widehat{\mathbf{x}}$ must satisfy the fixed-point condition (15) associated with the RED algorithms from [1], albeit with an MMSE-type denoiser. This restriction will be removed using the SMD framework in Section IV-C.

It is interesting to note that the gradient property (52) holds even for non-homogeneous $\widehat{\mathbf{f}}_{\text{mmse}, \nu}(\cdot)$. This generality is important in applications under which $\widehat{\mathbf{f}}_{\text{mmse}, \nu}(\cdot)$ is known to lack LH. For example, with a binary image $\mathbf{x} \in \{0, 1\}$ modeled by $\widehat{p}_{\mathbf{x}}(\mathbf{x}) = 0.5 \prod_{n=1}^N (\delta(x_n) + \delta(x_n - 1))$, the MMSE denoiser takes the form $[\widehat{\mathbf{f}}_{\text{mmse}, \nu}(\mathbf{x})]_n = 0.5 + 0.5 \tanh(x_n/\nu)$, which is not LH.

B. RLL as Kernel Density Estimation

We now show that regularization by log-likelihood (RLL) arises naturally in the data-driven, non-parametric context through kernel-density estimation (KDE) [8].

Recall that, in most imaging applications, the true prior $p_{\mathbf{x}}$ is unknown, as is the true MMSE denoiser $\mathbf{f}_{\text{mmse}, \nu}(\cdot)$. There are several ways to proceed. One way is to design "by hand" an approximate prior $\widehat{p}_{\mathbf{x}}$ that leads to a computationally efficient denoiser $\widehat{\mathbf{f}}_{\text{mmse}, \nu}(\cdot)$. But, because this denoiser is not MMSE for $\mathbf{x} \sim p_{\mathbf{x}}$, the performance of the resulting estimates $\widehat{\mathbf{x}}$ will suffer relative to $\mathbf{f}_{\text{mmse}, \nu}$.

Another way to proceed is to approximate the prior using a large corpus of training data $\{\mathbf{x}_t\}_{t=1}^T$. To this end, an approximate prior could be formed using the empirical estimate

$$\widehat{p}_{\mathbf{x}}(\mathbf{x}) = \frac{1}{T} \sum_{t=1}^T \delta(\mathbf{x} - \mathbf{x}_t), \quad (59)$$

but a much better (and smoother) match to the true prior $p_{\mathbf{x}}$ can be obtained using

$$\widetilde{p}_{\mathbf{x}}(\mathbf{x}; \nu) = \frac{1}{T} \sum_{t=1}^T \mathcal{N}(\mathbf{x}; \mathbf{x}_t, \nu \mathbf{I}) \quad (60)$$

with appropriately chosen $\nu > 0$, a technique known as kernel density estimation (KDE) or Parzen windowing [8]. Note that

if $\widetilde{p}_{\mathbf{x}}$ is used as a surrogate for $p_{\mathbf{x}}$, then the MAP optimization problem becomes

$$\widehat{\mathbf{x}} = \arg \min_{\mathbf{r}} \frac{1}{2\sigma^2} \|\mathbf{A}\mathbf{r} - \mathbf{y}\|^2 - \ln \widetilde{p}_{\mathbf{x}}(\mathbf{r}; \nu) \quad (61)$$

$$= \arg \min_{\mathbf{r}} \frac{1}{2\sigma^2} \|\mathbf{A}\mathbf{r} - \mathbf{y}\|^2 + \lambda \rho_{\text{LL}}(\mathbf{r}; \nu) \text{ for } \lambda = \frac{1}{\nu}, \quad (62)$$

with $\rho_{\text{LL}}(\cdot; \nu)$ constructed using $\widehat{p}_{\mathbf{x}}$ from (59). In summary, RLL arises naturally in the data-driven approach to image recovery when KDE is used to smooth the empirical prior.

C. Score-Matching by Denoising

A limitation of the above RLL framework is that it results in denoisers $\widehat{\mathbf{f}}_{\text{mmse}, \nu}$ with symmetric Jacobians. (Recall the discussion of MMSE denoisers in Section III-D.) To justify the use of RED algorithms with non-symmetric Jacobians, we introduce the *score-matching by denoising* (SMD) framework in this section.

Let us continue with the KDE-based MAP estimation problem (61). Note that $\widehat{\mathbf{x}}$ from (61) zeros the gradient of the MAP optimization objective and thus obeys the fixed-point equation

$$\frac{1}{\sigma^2} \mathbf{A}^\top (\mathbf{A}\widehat{\mathbf{x}} - \mathbf{y}) - \nabla \ln \widetilde{p}_{\mathbf{x}}(\widehat{\mathbf{x}}; \nu) = \mathbf{0}. \quad (63)$$

In principle, $\widehat{\mathbf{x}}$ in (63) could be found using gradient descent or similar techniques. However, computation of the gradient

$$\nabla \ln \widetilde{p}_{\mathbf{x}}(\mathbf{r}; \nu) = \frac{\nabla \widetilde{p}_{\mathbf{x}}(\mathbf{r}; \nu)}{\widetilde{p}_{\mathbf{x}}(\mathbf{r}; \nu)} = \frac{\sum_{t=1}^T (\mathbf{x}_t - \mathbf{r}) \mathcal{N}(\mathbf{r}; \mathbf{x}_t, \nu \mathbf{I})}{\nu \sum_{t=1}^T \mathcal{N}(\mathbf{r}; \mathbf{x}_t, \nu \mathbf{I})} \quad (64)$$

is too expensive for the values of T typically needed to generate a good image prior $\widetilde{p}_{\mathbf{x}}$.

A tractable alternative is suggested by the fact that

$$\nabla \ln \widetilde{p}_{\mathbf{x}}(\mathbf{r}; \nu) = \frac{\widehat{\mathbf{f}}_{\text{mmse}, \nu}(\mathbf{r}) - \mathbf{r}}{\nu} \quad (65)$$

$$\text{for } \widehat{\mathbf{f}}_{\text{mmse}, \nu}(\mathbf{r}) = \frac{\sum_{t=1}^T (\mathbf{x}_t - \mathbf{r}) \mathcal{N}(\mathbf{r}; \mathbf{x}_t, \nu \mathbf{I})}{\sum_{t=1}^T \mathcal{N}(\mathbf{r}; \mathbf{x}_t, \nu \mathbf{I})}, \quad (66)$$

where $\widehat{\mathbf{f}}_{\text{mmse}, \nu}(\mathbf{r})$ is the MMSE estimator of $\mathbf{x} \sim \widehat{p}_{\mathbf{x}}$ from $\mathbf{r} = \mathbf{x} + \mathcal{N}(\mathbf{0}, \nu \mathbf{I})$. In particular, if we can construct a good approximation to $\widehat{\mathbf{f}}_{\text{mmse}, \nu}(\cdot)$ using a denoiser $\mathbf{f}_{\theta}(\cdot)$ in a computationally efficient function class $\mathcal{F} \triangleq \{\mathbf{f}_{\theta} : \theta \in \Theta\}$, then we can efficiently approximate the MAP problem (61).

This approach can be formalized using the framework of *score matching* [29], which aims to approximate the "score" (i.e., the gradient of the log-prior) rather than the prior itself. For example, suppose that we want to want to approximate the score $\nabla \ln \widetilde{p}_{\mathbf{x}}(\cdot; \nu)$. For this, Hyvärinen [29] suggested to first find the best mean-square fit among a set of computationally efficient functions $\psi(\cdot; \theta)$, i.e., find

$$\widehat{\boldsymbol{\theta}} = \arg \min_{\boldsymbol{\theta}} \mathbb{E}_{\widetilde{p}_{\mathbf{x}}} \left\{ \|\psi(\mathbf{x}; \boldsymbol{\theta}) - \nabla \ln \widetilde{p}_{\mathbf{x}}(\mathbf{x}; \nu)\|^2 \right\}, \quad (67)$$

and then to approximate the score $\nabla \ln \widetilde{p}_{\mathbf{x}}(\cdot; \nu)$ by $\psi(\cdot; \widehat{\boldsymbol{\theta}})$. Later, in the context of denoising autoencoders, Vincent [30] showed that if we choose

$$\psi(\mathbf{x}; \boldsymbol{\theta}) = \frac{\mathbf{f}_{\boldsymbol{\theta}}(\mathbf{x}) - \mathbf{x}}{\nu} \quad (68)$$

for some function $f_\theta(\cdot) \in \mathcal{F}$, then $\hat{\theta}$ from (67) can be equivalently written as

$$\hat{\theta} = \arg \min_{\theta} \mathbb{E}_{\hat{p}_x} \left\{ \|f_\theta(x + \mathcal{N}(0, \nu I)) - x\|^2 \right\}. \quad (69)$$

In this case, $f_{\hat{\theta}}(\cdot)$ is the MSE-optimal denoiser, averaged over \hat{p}_x and constrained to the function class \mathcal{F} .

Plugging the score approximation (68) into the fixed-point condition (63), we get

$$\frac{1}{\sigma^2} \mathbf{A}^\top (\mathbf{A} \hat{x} - \mathbf{y}) + \lambda (\hat{x} - f_\theta(\hat{x})) = \mathbf{0} \text{ for } \lambda = \frac{1}{\nu}, \quad (70)$$

which matches the fixed-point condition (15) of the RED algorithms from [1]. Here we emphasize that \mathcal{F} may be constructed in such a way that $f_\theta(\cdot)$ has a non-symmetric Jacobian, which is the case for many state-of-the-art denoisers. Also, θ does not need to be optimized for (70) to hold. Finally, \hat{p}_x need not be the empirical prior (59); it can be any chosen prior [30]. Thus, the score-matching-by-denoising (SMD) framework offers an explanation of the RED algorithms from [1] that holds for generic denoisers $f_\theta(\cdot)$, whether or not they have symmetric Jacobians, are locally homogeneous, or MMSE. Furthermore, it suggests a rationale for choosing the regularization weight λ and, in the context of KDE, the denoiser variance ν .

D. Relation to Existing Work

Recently, Alain and Bengio [31] studied the contractive auto-encoders, a type of autoencoder that minimizes squared reconstruction error plus a penalty that tries to make the autoencoder as simple as possible. While previous works such as [32] conjectured that such auto-encoders minimize an energy function, Alain and Bengio showed that they actually minimize the norm of a score (i.e., match a score to zero). Furthermore, they showed that, when the coder and decoder do not share the same weights, it is not possible to define a valid energy function because the Jacobian of the reconstruction function is not symmetric. The results in [31] parallel those in this paper, except that they focus on auto-encoders while we focus on variational image recovery. Another small difference is that [31] uses the small- ν approximation

$$\hat{f}_{\text{mmse}, \nu}(x) = x + \nu \nabla \ln \hat{p}_x(x) + o(\nu), \quad (71)$$

whereas we use the exact (Tweedie's) relationship (52), i.e.,

$$\hat{f}_{\text{mmse}, \nu}(x) = x + \nu \nabla \ln \tilde{p}_x(x), \quad (72)$$

where \tilde{p}_x is the “Gaussian blurred” version of \hat{p}_x from (50).

V. FAST RED ALGORITHMS

In [1], Romano et al. proposed several ways to solve the fixed-point equation (15). Throughout our paper, we have been referring to these methods as “RED algorithms.” In this section, we provide new interpretations of the RED-ADMM and RED-FP algorithms from [1] and we propose new RED algorithms based on Peaceman-Rachford splitting, expectation-consistent approximation, and majorization minimization.

Algorithm 2 RED-ADMM [1]

Require: $\ell(\cdot; \mathbf{y}), \mathbf{f}(\cdot), \beta, \lambda, \mathbf{v}_0, \mathbf{u}_0, K$, and I

```

1: for  $k = 1, 2, \dots, K$  do
2:    $\mathbf{x}_k = \arg \min_{\mathbf{x}} \{ \ell(\mathbf{x}; \mathbf{y}) + \frac{\beta}{2} \|\mathbf{x} - \mathbf{v}_{k-1} + \mathbf{u}_{k-1}\|^2 \}$ 
3:    $\mathbf{z}_0 = \mathbf{v}_{k-1}$ 
4:   for  $i = 1, 2, \dots, I$  do
5:      $\mathbf{z}_i = \frac{\lambda}{\lambda + \beta} \mathbf{f}(\mathbf{z}_{i-1}) + \frac{\beta}{\lambda + \beta} (\mathbf{x}_k + \mathbf{u}_{k-1})$ 
6:   end for
7:    $\mathbf{v}_k = \mathbf{z}_I$ 
8:    $\mathbf{u}_k = \mathbf{u}_{k-1} + \mathbf{x}_k - \mathbf{v}_k$ 
9: end for
10: Return  $\mathbf{x}_K$ 

```

A. RED-ADMM

The ADMM approach was summarized in Algorithm 1 for an arbitrary regularizer $\rho(\cdot)$. To apply ADMM to RED, line 3 of Algorithm 1, known as the “proximal update,” must be specialized to the case where $\rho(\cdot)$ obeys (13) for some denoiser $\mathbf{f}(\cdot)$. To do this, Romano et al. [1] proposed the following. Because $\rho(\cdot)$ is differentiable, the proximal solution \mathbf{v}_k must obey the fixed-point relationship

$$\mathbf{0} = \lambda \nabla \rho(\mathbf{v}_k) + \beta(\mathbf{v}_k - \mathbf{x}_k - \mathbf{u}_{k-1}) \quad (73)$$

$$= \lambda(\mathbf{v}_k - \mathbf{f}(\mathbf{v}_k)) + \beta(\mathbf{v}_k - \mathbf{x}_k - \mathbf{u}_{k-1}) \quad (74)$$

$$\Leftrightarrow \mathbf{v}_k = \frac{\lambda}{\lambda + \beta} \mathbf{f}(\mathbf{v}_k) + \frac{\beta}{\lambda + \beta} (\mathbf{x}_k + \mathbf{u}_{k-1}). \quad (75)$$

An approximation to \mathbf{v}_k can thus be obtained by iterating

$$\mathbf{z}_i = \frac{\lambda}{\lambda + \beta} \mathbf{f}(\mathbf{z}_{i-1}) + \frac{\beta}{\lambda + \beta} (\mathbf{x}_k + \mathbf{u}_{k-1}) \quad (76)$$

over $i = 1, \dots, I$ with sufficiently large I , initialized at $\mathbf{z}_0 = \mathbf{v}_{k-1}$. This procedure is detailed in lines 3-6 of Algorithm 2. The overall algorithm is known as RED-ADMM.

B. Inexact RED-ADMM

Algorithm 2 faithfully implements ADMM when the number of inner iterations, I , is sufficiently large. But using many inner iterations may be impractical when the denoiser is computationally expensive, as in the case of BM3D or TNRD. Furthermore, it is not clear that the use of many inner iterations is necessary.

For example, Fig. 2 plots PSNR trajectories for $I = 1, 2, 3, 4$ inner iterations. For this experiment, we used the deblurring problem described in Section V-G (see that section for details), but a similar behavior can be observed in other RED applications. Figure 2 suggests that $I = 1$ is optimal, leading to the simplified approach in Algorithm 3. Note that [1] also focused on $I = 1$ when implementing RED-ADMM.

With only a single inner iteration, Algorithm 3 seems only distantly related to ADMM. The question is whether there exists a better interpretation. Noting that line 3 of Algorithm 3 can be rewritten as

$$\mathbf{v}_k = \mathbf{v}_{k-1} - \frac{1}{\lambda + \beta} [\lambda \nabla \rho(\mathbf{v}_{k-1}) + \beta(\mathbf{v}_{k-1} - \mathbf{x}_k - \mathbf{u}_{k-1})] \quad (77)$$

$$= \mathbf{v}_{k-1} - \frac{1}{\lambda + \beta} \nabla \left[\lambda \rho(\mathbf{v}) + \frac{\beta}{2} \|\mathbf{v} - \mathbf{x}_k - \mathbf{u}_{k-1}\|^2 \right]_{\mathbf{v}=\mathbf{v}_{k-1}} \quad (78)$$

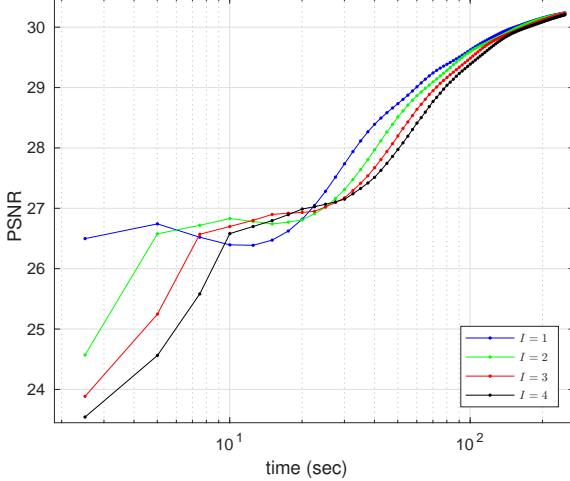


Fig. 2. PSNR versus runtime for RED-ADMM with I inner iterations.

Algorithm 3 RED-ADMM with $I = 1$

Require: $\ell(\cdot; \mathbf{y}), \mathbf{f}(\cdot), \beta, \lambda, \mathbf{v}_0, \mathbf{u}_0$, and K

- 1: **for** $k = 1, 2, \dots, K$ **do**
- 2: $\mathbf{x}_k = \arg \min_{\mathbf{x}} \{\ell(\mathbf{x}; \mathbf{y}) + \frac{\beta}{2} \|\mathbf{x} - \mathbf{v}_{k-1} + \mathbf{u}_{k-1}\|^2\}$
- 3: $\mathbf{v}_k = \frac{\lambda}{\lambda + \beta} \mathbf{f}(\mathbf{v}_{k-1}) + \frac{\beta}{\lambda + \beta} (\mathbf{x}_k + \mathbf{u}_{k-1})$
- 4: $\mathbf{u}_k = \mathbf{u}_{k-1} + \mathbf{x}_k - \mathbf{v}_k$
- 5: **end for**
- 6: Return \mathbf{x}_K

we see that, when $I = 1$, RED-ADMM replaces the proximal step with a gradient-descent step under stepsize $1/(\lambda + \beta)$. Thus this inexact-ADMM algorithm has connections to the well-known proximal gradient algorithm [33]. We will have more to say about this connection in the sequel.

C. Inexact Peaceman-Rachford Splitting

ADMM is known to be equivalent to Douglas-Rachford splitting on the dual objective [11]. If Peaceman-Rachford splitting (PRS) is instead applied on the dual, then the resulting primal algorithm is similar to ADMM but includes a second dual update “ $\mathbf{u}_{k-\frac{1}{2}} = \mathbf{u}_{k-1} + \mathbf{x}_k - \mathbf{v}_{k-1}$ ” between lines 2 and 3 of Algorithm 1 [11]. The PRS-based approach is said to converge faster than ADMM, although at the expense of more restrictive convergence conditions [34].

This PRS-based approach can be applied to RED by simply adding a second dual update between lines 2-3 of RED-ADMM (i.e., Algorithm 2). Implementing this algorithm with $I = 1$ inner iterations then yields the approach summarized in Algorithm 4. As we show in the sequel, this “RED-PRS” approach is indeed a bit faster than RED-ADMM.

D. Inexact GEC

A version of *generalized expectation-consistent approximate inference* (GEC) applicable to Bayesian MAP estimation

Algorithm 4 RED-PRS with $I = 1$

Require: $\ell(\cdot; \mathbf{y}), \mathbf{f}(\cdot), \beta, \lambda, \mathbf{v}_0, \mathbf{u}_0$, and K

- 1: **for** $k = 1, 2, \dots, K$ **do**
- 2: $\mathbf{x}_k = \arg \min_{\mathbf{x}} \{\ell(\mathbf{x}; \mathbf{y}) + \frac{\beta}{2} \|\mathbf{x} - \mathbf{v}_{k-1} + \mathbf{u}_{k-1}\|^2\}$
- 3: $\mathbf{u}_{k-\frac{1}{2}} = \mathbf{u}_{k-1} + \mathbf{x}_k - \mathbf{v}_{k-1}$
- 4: $\mathbf{v}_k = \frac{\lambda}{\lambda + \beta} \mathbf{f}(\mathbf{v}_{k-1}) + \frac{\beta}{\lambda + \beta} (\mathbf{x}_k + \mathbf{u}_{k-\frac{1}{2}})$
- 5: $\mathbf{u}_k = \mathbf{u}_{k-\frac{1}{2}} + \mathbf{x}_k - \mathbf{v}_k$
- 6: **end for**
- 7: Return \mathbf{x}_K

Algorithm 5 GEC [35]

Require: $\mathbf{g}_1(\cdot; \cdot), \mathbf{g}_2(\cdot; \cdot), \mathbf{r}_1, \beta_1, \xi \in (0, 1]$, and K

- 1: **for** $k = 1, 2, \dots, K$ **do**
- 2: $\mathbf{x} \leftarrow \mathbf{g}_1(\mathbf{r}_1; \beta_1)$
- 3: $\eta_1 \leftarrow \beta_1 N / \text{tr} [J \mathbf{g}_1(\mathbf{r}_1; \beta_1)]$
- 4: $\beta_2 \leftarrow \eta_1 - \beta_1$
- 5: $\mathbf{r}_2 \leftarrow (\eta_1 \mathbf{x} - \beta_1 \mathbf{r}_1) / \beta_2$
- 6: $\mathbf{v} \leftarrow \mathbf{g}_2(\mathbf{r}_2; \beta_2)$
- 7: $\eta_2 \leftarrow \beta_2 N / \text{tr} [J \mathbf{g}_2(\mathbf{r}_2; \beta_2)]$
- 8: $\beta_1 \leftarrow \xi(\eta_2 - \beta_2) + (1 - \xi)\beta_1$
- 9: $\mathbf{r}_1 \leftarrow (\eta_2 \mathbf{v} - \beta_2 \mathbf{r}_2) / \beta_1$
- 10: **end for**
- 11: Return \mathbf{x}

was proposed in [35]. GEC is summarized in Algorithm 5 using the estimation functions

$$\mathbf{g}_1(\mathbf{r}_1; \beta_1) = \arg \min_{\mathbf{x}} \left\{ \ell(\mathbf{x}; \mathbf{y}) + \frac{\beta_1}{2} \|\mathbf{x} - \mathbf{r}_1\|^2 \right\} \quad (79)$$

$$\mathbf{g}_2(\mathbf{r}_2; \beta_2) = \arg \min_{\mathbf{v}} \left\{ \lambda \rho(\mathbf{v}) + \frac{\beta_2}{2} \|\mathbf{v} - \mathbf{r}_2\|^2 \right\}. \quad (80)$$

For the quadratic loss $\frac{1}{2\sigma^2} \|\mathbf{A}\mathbf{x} - \mathbf{y}\|^2$, lines 2–3 of Algorithm 5 become

$$\mathbf{x} \leftarrow \left(\frac{1}{\sigma^2} \mathbf{A}^\top \mathbf{A} + \beta_1 \mathbf{I} \right)^{-1} \left(\frac{1}{\sigma^2} \mathbf{A}^\top \mathbf{y} + \beta_1 \mathbf{r}_1 \right) \quad (81)$$

$$\eta_1 \leftarrow \frac{N}{\text{tr}[(\mathbf{A}^\top \mathbf{A} / \sigma^2 + \beta_1 \mathbf{I})^{-1}]}, \quad (82)$$

and for a differentiable $\rho(\mathbf{x})$ with gradient in (13), line 6 of Algorithm 5 is a proximal update with the same form as line 3 of Algorithm 1. It can be shown that GEC is equivalent to PRS-ADMM, except that i) the value of β is allowed to differ between proximal steps and ii) these β values are adapted at each iteration k .

To apply GEC to RED, we approximate the second proximal step with the same technique used for ADMM. That is, we iterate (76) over $i = 1, \dots, I$, but with \mathbf{r}_2 in place of $\mathbf{x}_k + \mathbf{u}_{k-1}$. Again, we focus on the case of $I = 1$ inner iteration, yielding

$$\mathbf{v} \leftarrow \frac{\lambda}{\lambda + \beta_2} \mathbf{f}(\mathbf{v}) + \frac{\beta_2}{\lambda + \beta_2} \mathbf{r}_2 \quad (83)$$

$$\eta_2 \leftarrow \lambda + \beta_2. \quad (84)$$

As we show in the sequel, the resulting RED-GEC approach is indeed a bit faster than RED-ADMM and RED-PRS.

Algorithm 6 RED-PG-DP Algorithm

Require: $\ell(\cdot; \mathbf{y}), \mathbf{f}(\cdot), \lambda, \mathbf{v}_0, L_0, L_\infty$, and K

- 1: **for** $k = 1, 2, \dots, K$ **do**
- 2: $\mathbf{x}_k = \arg \min_{\mathbf{x}} \{\ell(\mathbf{x}; \mathbf{y}) + \frac{\lambda L_{k-1}}{2} \|\mathbf{x} - \mathbf{v}_{k-1}\|^2\}$
- 3: $L_k = \left(\frac{1}{L_\infty} + \left(\frac{1}{L_0} - \frac{1}{L_\infty} \right) \frac{1}{\sqrt{k+1}} \right)^{-1}$
- 4: $\mathbf{v}_k = \frac{1}{L_k} \mathbf{f}(\mathbf{x}_k) - \frac{1-L_k}{L_k} \mathbf{x}_k$
- 5: **end for**
- 6: Return \mathbf{x}_K

E. Proximal Gradient Algorithm with Dynamic Stepsize

We now propose a RED algorithm inspired by majorization minimization (MM) [36]. MM suggests to minimize a version of the variational objective (2) using a quadratic upper bound of the form

$$\bar{\rho}(\mathbf{x}; \mathbf{x}_k) \triangleq \rho(\mathbf{x}_k) + [\nabla \rho(\mathbf{x}_k)]^\top (\mathbf{x} - \mathbf{x}_k) + \frac{L}{2} \|\mathbf{x} - \mathbf{x}_k\|_2^2 \quad (85)$$

$$\geq \rho(\mathbf{x}) \quad \forall \mathbf{x} \in \mathcal{X}, \quad (86)$$

in place of $\rho(\mathbf{x})$ at the k th algorithm iteration. If $\nabla \rho(\cdot)$ is L -Lipschitz, then the upper bounding property is guaranteed. We then apply the proximal-gradient (PG) algorithm [33] (also known as forward-backward splitting) as follows. First notice from (85) that the upper-bounded objective can be written as

$$\ell(\mathbf{x}; \mathbf{y}) + \lambda \bar{\rho}(\mathbf{x}; \mathbf{x}_k) = \ell(\mathbf{x}; \mathbf{y}) + \frac{\lambda L}{2} \left\| \mathbf{x} - \left(\mathbf{x}_k - \frac{1}{L} \nabla \rho(\mathbf{x}_k) \right) \right\|^2 + \text{const} \quad (87)$$

$$= \ell(\mathbf{x}; \mathbf{y}) + \frac{\lambda L}{2} \underbrace{\left\| \mathbf{x} - \left(\mathbf{x}_k - \frac{1}{L} (\mathbf{x}_k - \mathbf{f}(\mathbf{x}_k)) \right) \right\|^2}_{\triangleq \mathbf{v}_k} + \text{const}, \quad (88)$$

where (88) follows from assuming (46), which is the basis for all RED algorithms. The PG algorithm then alternately updates \mathbf{v}_k as per the gradient step in (88) and updates \mathbf{x}_{k+1} according to the proximal step

$$\mathbf{x}_{k+1} = \arg \min_{\mathbf{x}} \left\{ \ell(\mathbf{x}; \mathbf{y}) + \frac{\lambda L}{2} \|\mathbf{x} - \mathbf{v}_k\|^2 \right\}. \quad (89)$$

Convergence conditions are discussed in [36].

In practice, we find that the algorithm converges faster if a smaller value of the penalty L is used for the early iterations k . Thus, using L_k to denote the value of L at iteration k , we suggest to choose the extreme values L_0 and L_∞ and smoothly interpolate between them for intermediate k . One way to do this is summarized in line 3 of Algorithm 6. We refer to this algorithm as PG with dynamic penalty (PG-DP).

There are interesting similarities between RED-PG and RED-ADMM- $I=1$: both alternate a proximal update on the loss with a gradient update on the regularization, where the latter term manifests as a convex combination between the denoiser output and another term. The main difference is that RED-ADMM- $I=1$ includes an extra state “ \mathbf{u}_k .”

F. RED-FP

We now show that RED-PG with $L_0 = L_\infty = 1$ is identical to the RED-FP algorithm from [1]. To see this, notice from Algorithm 6 that $\mathbf{v}_k = \mathbf{f}(\mathbf{x}_k)$ when $L_k = 1$, in which case

$$\mathbf{x}_k = \arg \min_{\mathbf{x}} \left\{ \ell(\mathbf{x}; \mathbf{y}) + \frac{\lambda}{2} \|\mathbf{x} - \mathbf{f}(\mathbf{x}_{k-1})\|^2 \right\}. \quad (90)$$

For the quadratic loss $\ell(\mathbf{x}; \mathbf{y}) = \frac{1}{2\sigma^2} \|\mathbf{Ax} - \mathbf{y}\|^2$, (90) becomes

$$\mathbf{x}_k = \arg \min_{\mathbf{x}} \left\{ \frac{1}{2\sigma^2} \|\mathbf{Ax} - \mathbf{y}\|^2 + \frac{\lambda}{2} \|\mathbf{x} - \mathbf{f}(\mathbf{x}_{k-1})\|^2 \right\} \quad (91)$$

$$= \left(\frac{1}{\sigma^2} \mathbf{A}^\top \mathbf{A} + \lambda \mathbf{I} \right)^{-1} \left(\frac{1}{\sigma^2} \mathbf{A}^\top \mathbf{y} + \lambda \mathbf{f}(\mathbf{x}_{k-1}) \right), \quad (92)$$

which is identical to the RED-FP update [1, (37)]. Thus, (90) is the generalization of the RED-FP algorithm from [1, (37)] to possibly non-quadratic² loss $\ell(\cdot; \mathbf{y})$, and the RED-PG algorithm is the generalization of (90) to $L_0 = L_\infty = 1$. In the sequel, we find that, with appropriate selection of L_0 and L_∞ , RED-PG is significantly faster than RED-FP.

G. Algorithm Comparison: Image Deblurring

We now compare the performance of the RED algorithms discussed above (i.e., ADMM, PRS, GEC, PG-DP, and FP) on the image deblurring problem considered in [1, Sec.6.1]. For this, the measurements \mathbf{y} were constructed using a 9×9 uniform blur kernel for \mathbf{A} and AWGN with variance $\sigma^2 = 2$. As stated earlier, the images \mathbf{x} were normalized to have pixel intensities in the range $[0, 255]$.

For this experiment, we used the TNRD denoiser. The various algorithmic parameters were chosen based on the recommendations in [1]: the denoiser variance was $\nu = 3.25^2$, the regularization weight was $\lambda = 0.02$, and the ADMM penalty parameter was $\beta = 0.001$. For the proximal step on $\rho(\mathbf{x})$, we used $I = 1$ inner iterations in ADMM, PRS, and GEC. For the proximal step on $\ell(\mathbf{x}; \mathbf{y})$ (e.g., (81)-(82) and (92)) we used an FFT. For the PG-DP approach, we used $L_0 = 0.2$ and $L_\infty = 2$.

Figure 3 shows PSNR $\triangleq -10 \log_{10} (\frac{1}{N \cdot 256^2} \|\mathbf{x} - \hat{\mathbf{x}}\|^2)$ versus runtime averaged over the 16 test images (of size 256×256) listed in footnote 1. The figure shows that the proposed RED-PG-DP algorithm is about twice as fast as the other algorithms in achieving any PSNR ≥ 27 . Among the other algorithms, there is little difference in runtime to reach the highest PSNRs, and small differences to reach mid-range PSNRs like 27 or 28. To reach these mid-range PSNRs, PRS is slightly faster than ADMM (as expected from [34]), and GEC is slightly faster than PRS (as expected from β adaptation).

We emphasize that the RED-PRS, RED-GEC, and RED-PG-DP algorithms proposed in this paper solve the same fixed-point equation (15) that was solved by the RED-SD, RED-ADMM, and RED-FP algorithms from [1]. The excellent quality of the resulting fixed-points was firmly established in [1], both qualitatively and quantitatively, and in comparison to existing state-of-the-art methods like PnP-ADMM [9]. For

²The extension to non-quadratic loss is important for applications like phase-retrieval, where RED has been successfully applied [37].

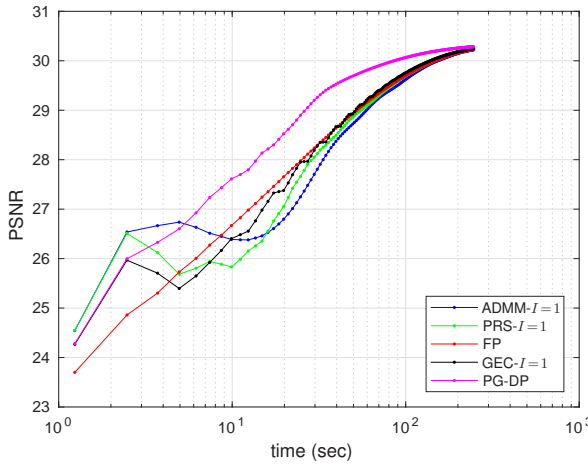


Fig. 3. Average PSNR versus runtime on the deblurring problem described in the text. The reported PSNR is the average over 16 test images.

further details on these comparisons, including examples of recovered images, we refer the interested reader to [1].

VI. CONCLUSION

The RED paper [1] proposed a powerful new way to exploit plug-in denoisers when solving imaging inverse-problems. In fact, experiments in [1] suggest that the RED algorithms are state-of-the-art. A closer look into the behavior of these algorithms, however, calls into question the central claim in [1], which is that the RED algorithms minimize an objective containing an explicit regularization of the form $\rho_{\text{red}}(\mathbf{x}) \triangleq \frac{1}{2}\mathbf{x}^\top(\mathbf{x} - \mathbf{f}(\mathbf{x}))$. In this paper, we established that explicit regularization by $\rho_{\text{red}}(\mathbf{x})$ explains the RED algorithms only in the case that the denoiser $\mathbf{f}(\cdot)$ has both i) Jacobian symmetry (JS) and ii) a very high degree of local homogeneity (LH). Our experiments suggest that these two conditions are not simultaneously satisfied by practical denoisers such as the median filter, non-local means, BM3D, TNRD, or DnCNN. Furthermore, we established that RED algorithms with non-JS denoisers cannot be explained by explicit regularization of any form.

In light of these results, there remains the question of how to understand the excellent performance of RED algorithms with practical (i.e., non-LH and/or non-JS) denoisers. In response, we showed that the RED algorithms can be explained by a novel framework called “score-matching by denoising” (SMD), which aims to match the *score* (i.e., the gradient of the log-prior) rather than to design any explicit regularizer. We then established tight connections between SMD, kernel density estimation, and constrained MMSE denoising.

Finally, we provided new interpretations of the RED-ADMM and RED-FP algorithms proposed in [1], and we proposed novel RED algorithms with faster convergence.

ACKNOWLEDGMENTS

The authors thank Peyman Milanfar and Miki Elad for inspiration and insightful discussions.

REFERENCES

- [1] Y. Romano, M. Elad, and P. Milanfar, “The little engine that could: Regularization by denoising (RED),” *SIAM J. Imag. Sci.*, vol. 10, no. 4, pp. 1804–1844, 2017.
- [2] A. Buades, B. Coll, and J.-M. Morel, “A review of image denoising algorithms, with a new one,” *Multiscale Model. Sim.*, vol. 4, no. 2, pp. 490–530, 2005.
- [3] P. Milanfar, “A tour of modern image filtering: New insights and methods, both practical and theoretical,” *IEEE Signal Process. Mag.*, vol. 30, no. 1, pp. 106–128, 2013.
- [4] A. Buades, B. Coll, and J.-M. Morel, “A non-local algorithm for image denoising,” in *Proc. IEEE Conf. Comp. Vision Pattern Recog.*, vol. 2, pp. 60–65, 2005.
- [5] K. Dabov, A. Foi, V. Katkovnik, and K. Egiazarian, “Image denoising by sparse 3-D transform-domain collaborative filtering,” *IEEE Trans. Image Process.*, vol. 16, no. 8, pp. 2080–2095, 2007.
- [6] Y. Chen and T. Pock, “Trainable nonlinear reaction diffusion: A flexible framework for fast and effective image restoration,” *IEEE Trans. Pattern Anal. Mach. Intell.*, vol. 39, no. 6, pp. 1256–1272, 2017.
- [7] K. Zhang, W. Zuo, Y. Chen, D. Meng, and L. Zhang, “Beyond a Gaussian denoiser: Residual learning of deep CNN for image denoising,” *IEEE Trans. Image Process.*, vol. 26, no. 7, pp. 3142–3155, 2017.
- [8] E. Parzen, “On estimation of a probability density function and mode,” *Ann. Math. Statist.*, vol. 33, no. 3, pp. 1065–1076, 1962.
- [9] S. V. Venkatakrishnan, C. A. Bouman, and B. Wohlberg, “Plug-and-play priors for model based reconstruction,” p. 945948, 2013.
- [10] C. M. Bishop, *Pattern Recognition and Machine Learning*. New York: Springer, 2007.
- [11] S. Boyd, N. Parikh, E. Chu, B. Peleato, and J. Eckstein, “Distributed optimization and statistical learning via the alternating direction method of multipliers,” *Found. Trends Mach. Learn.*, vol. 3, no. 1, pp. 1–122, 2011.
- [12] D. L. Donoho, A. Maleki, and A. Montanari, “Message passing algorithms for compressed sensing,” *Proc. Nat. Acad. Sci.*, vol. 106, pp. 18914–18919, Nov. 2009.
- [13] C. A. Metzler, A. Maleki, and R. G. Baraniuk, “BM3D-AMP: A new image recovery algorithm based on BM3D denoising,” in *Proc. IEEE Int. Conf. Image Process.*, pp. 3116–3120, 2015.
- [14] P. Schniter, S. Rangan, and A. K. Fletcher, “Denoising-based vector approximate message passing,” in *Proc. Int'l. Biomed. Astronom. Signal Process. (BASP) Frontiers Workshop*, 2017.
- [15] R. Berthier, A. Montanari, and P.-M. Nguyen, “State evolution for approximate message passing with non-separable functions,” *arXiv:1708.03950*, 2017.
- [16] A. K. Fletcher, S. Rangan, S. Sarkar, and P. Schniter, “Plug-in estimation in high-dimensional linear inverse problems: A rigorous analysis,” 2018.
- [17] T. S. Huang, G. J. Yang, and Y. T. Tang, “A fast two-dimensional median filtering algorithm,” *IEEE Trans. Acoust. Speech & Signal Process.*, vol. 27, no. 1, pp. 13–18, 1979.
- [18] W. Rudin, *Principles of Mathematical Analysis*. New York: McGraw-Hill, 3rd ed., 1976.
- [19] S. Kantorovitz, *Several Real Variables*. Springer, 2016.
- [20] D. L. Donoho and I. M. Johnstone, “Ideal spatial adaptation by wavelet shrinkage,” *Biometrika*, vol. 81, no. 3, pp. 425–455, 1994.
- [21] R. R. Coifman and D. L. Donoho, “Translation-invariant de-noising,” in *Wavelets and Statistics* (A. Antoniadis and G. Oppenheim, eds.), pp. 125–150, Springer, 1995.
- [22] N. Parikh and S. Boyd, “Proximal algorithms,” vol. 3, no. 1, pp. 123–231, 2013.
- [23] A. Teodoro, J. M. Bioucas-Dias, and M. A. T. Figueiredo, “Scene-adapted plug-and-play algorithm with guaranteed convergence: Applications to data fusion in imaging,” *arXiv:1801.00605*, 2018.
- [24] P. Milanfar, “Symmetrizing smoothing filters,” *SIAM J. Imag. Sci.*, vol. 30, no. 1, pp. 263–284, 2013.
- [25] P. Milanfar and H. Talebi, “A new class of image filters without normalization,” in *Proc. IEEE Int. Conf. Image Process.*, pp. 3294–3298, 2016.
- [26] T. Goldstein, C. Studer, and R. Baraniuk, “Forward-backward splitting with a FASTA implementation,” *arXiv:1411.3406*, 2014.
- [27] H. Robbins, “An empirical Bayes approach to statistics,” in *Proc. Berkeley Symp. Math. Stats. Prob.*, pp. 157–163, 1956.
- [28] B. Efron, “Tweedie's formula and selection bias,” *J. Am. Statist. Assoc.*, vol. 106, no. 496, pp. 1602–1614, 2011.
- [29] A. Hyvärinen, “Estimation of non-normalized statistical models by score matching,” *J. Mach. Learn. Res.*, vol. 6, pp. 695–709, 2005.

- [30] P. Vincent, “A connection between score matching and denoising autoencoders,” *Neural Comput.*, vol. 23, no. 7, pp. 1661–1674, 2011.
- [31] G. Alain and Y. Bengio, “What regularized auto-encoders learn from the data-generating distribution,” *J. Mach. Learn. Res.*, vol. 15, no. 1, pp. 3563–3593, 2014.
- [32] M. A. Ranzato, Y.-L. Boureau, and Y. LeCun, “Sparse feature learning for deep belief networks,” in *Proc. Neural Inform. Process. Syst. Conf.*, pp. 1185–1192, 2008.
- [33] P. L. Combettes and J.-C. Pesquet, “Proximal splitting methods in signal processing,” in *Fixed-Point Algorithms for Inverse Problems in Science and Engineering* (H. Bauschke, R. Burachik, P. Combettes, V. Elser, D. Luke, and H. Wolkowicz, eds.), pp. 185–212, Springer, 2011.
- [34] B. He, H. Liu, Z. Wang, and X. Yuan, “A strictly contractive Peaceman-Rachford splitting method for convex programming,” *SIAM J. Optim.*, vol. 24, no. 3, pp. 1011–1040, 2014.
- [35] A. K. Fletcher, M. Sahraee-Ardakan, S. Rangan, and P. Schniter, “Expectation consistent approximate inference: Generalizations and convergence,” in *Proc. IEEE Int. Symp. Inform. Thy.*, pp. 190–194, 2016.
- [36] Y. Sun, P. Babu, and D. P. Palomar, “Majorization-minimization algorithms in signal processing, communications, and machine learning,” *IEEE Trans. Signal Process.*, vol. 65, no. 3, pp. 794–816, 2017.
- [37] C. A. Metzler, P. Schniter, A. Veeraraghavan, and R. G. Baraniuk, “prDeep: Robust phase retrieval with flexible deep neural networks,” in *Proc. Int. Conf. Mach. Learning*, 2018 (see also arXiv:1803:00212).